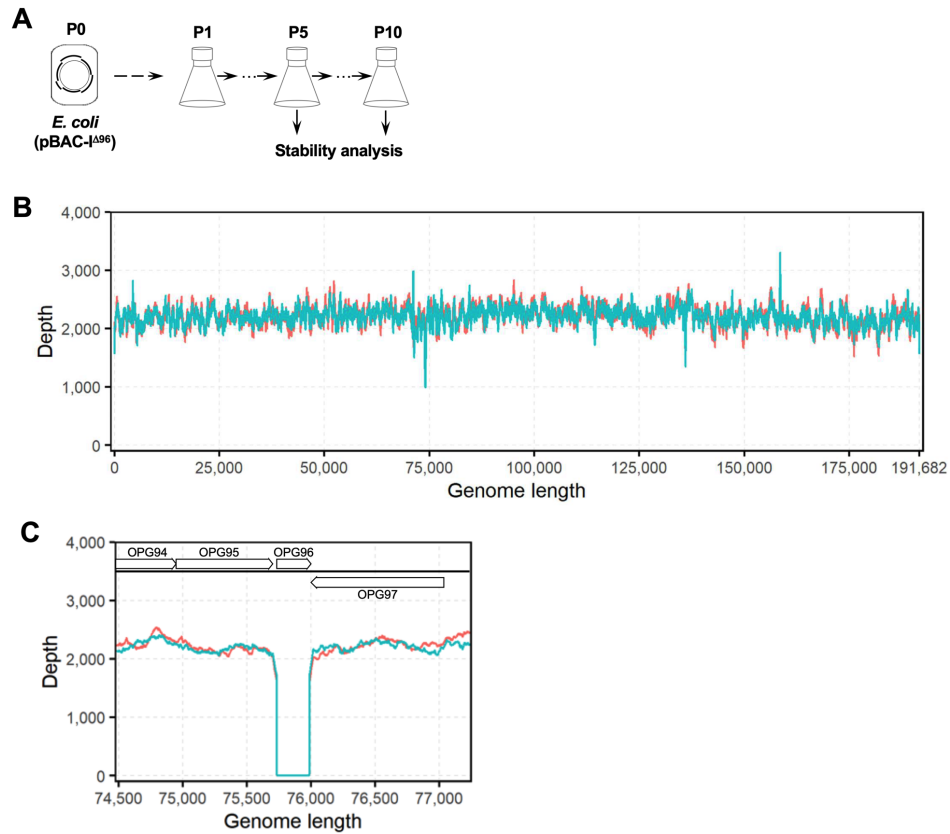


SUPPLEMENTARY INFORMATION

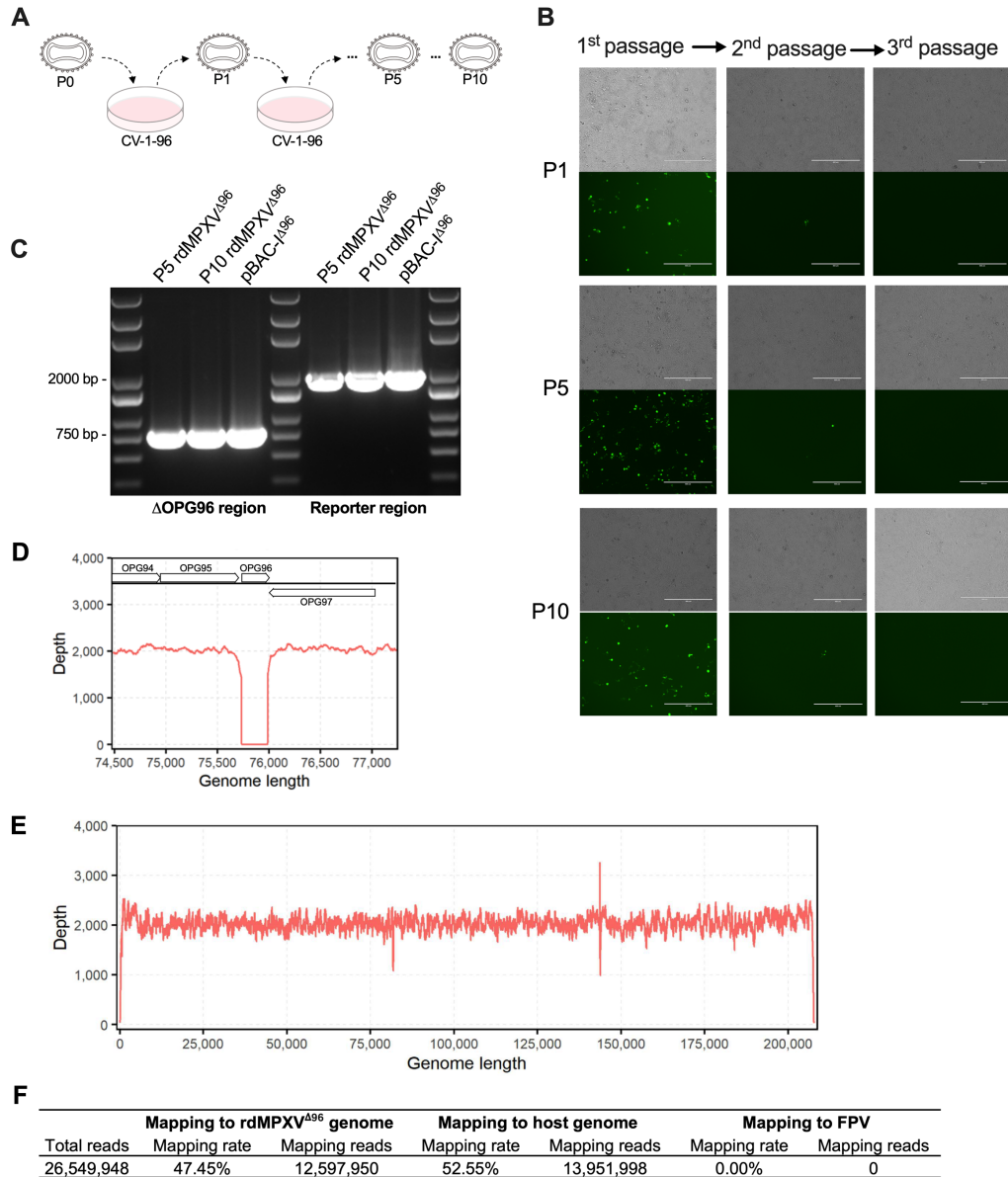
Development of a replication-defective monkeypox virus platform for fundamental and therapeutic research

Jiannan Chen^{1, 2§}, Liyuan Hu^{1§}, Riccardo Vernuccio^{3§}, Ning Shi^{4§}, Jiaxin Tian⁵, Yuyi Zhang¹, Sicheng Tian¹, Xinyu Cao⁵, Zhuo Ha⁵, Jiahan Lu⁶, Leandro Battini³, Bertrand Raynal⁷, Ahmed Haouz⁸, Jing Xue⁶, Qiliang Cai¹, Yiqi Zhao⁹, Yongxu Lu¹⁰, Geoffrey L. Smith^{9,10,11}, Youhua Xie^{1*}, Huijun Lu^{5*}, Pablo Guardado-Calvo^{3*}, Ping Zhang^{2*}, and Rong Zhang^{1*}



Supplementary Figure 1. Stability analysis of the pBAC-I^{Δ96} plasmid.

A. Schematic diagram of pBAC-I propagation in *E. coli* across generations. **B.** Read depth of *E. coli*-derived P5 (red line) and P10 (green line) of pBAC-I^{Δ96} aligned to the pBAC-I^{Δ96} reference sequences. **C.** Read depth of *E. coli*-derived P5 (red line) and P10 (green line) of pBAC-I^{Δ96} aligned to MPXV reference genome, with focus on OPG96 (gene *M2R*) and flanking regions. After filtering and pairing, the reads were aligned to the designed plasmid reference using the BWA software (version 0.7.18) with default parameters ⁷⁷. The coverage across different regions of the plasmid was then calculated using the bam-readcount tool ⁷⁸, and the data were visualized using R.



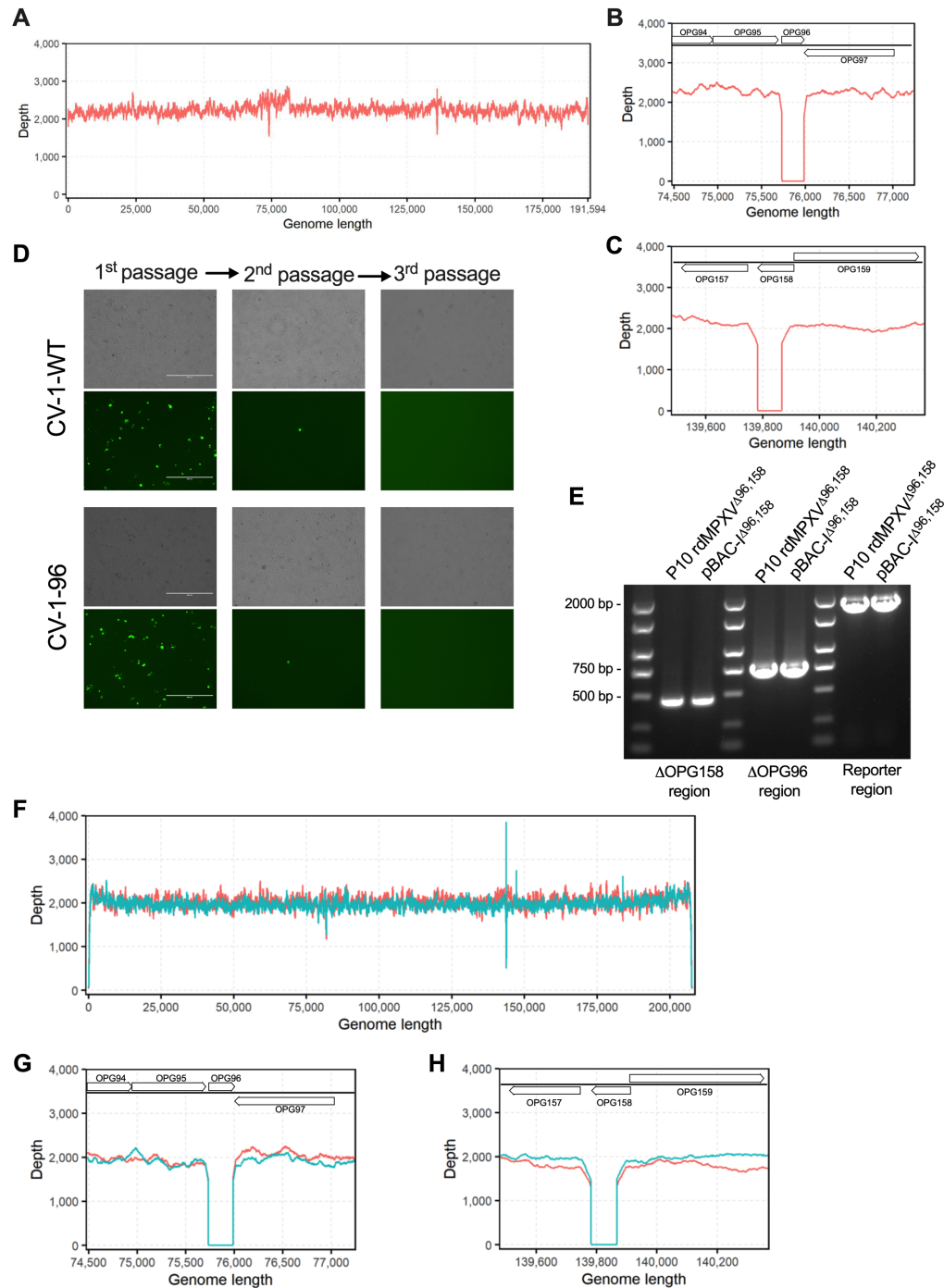
Supplementary Figure 2. Stability of rdMPXV^{Δ96} upon serial passaging.

A. Schematic of serial passaging of rdMPXV^{Δ96} in CV-1-96 cells. The P0 virus (harvested from CV-1-M cells transfected with pBAC-MPXV^{Δ96}) was used to infect fresh CV-1-96 cells, yielding P1. Similarly, P5 and P10 viruses were obtained. **B.** Serial passaging of rdMPXV^{Δ96} in CV-1-WT cells. P1, P5, and P10 viruses from CV-1-96 cells (panel A) were passaged for three rounds in CV-1-WT cells. Brightfield and fluorescent images were captured at 96 h post-infection. Scale bar, 400 μm. **C.** PCR-based detection of the OPG96-deleted region and mGreenLantern-P2A-Gaussia luciferase reporter cassette in P5 and P10 rdMPXV^{Δ96}. Viral genomic DNA from P5 and P10 was amplified by PCR, with pBAC-I^{Δ96} as a positive control. **D.** Read depth of P5 rdMPXV^{Δ96}

aligned to MPXV reference genome, focusing on *OPG96* and flanking regions.

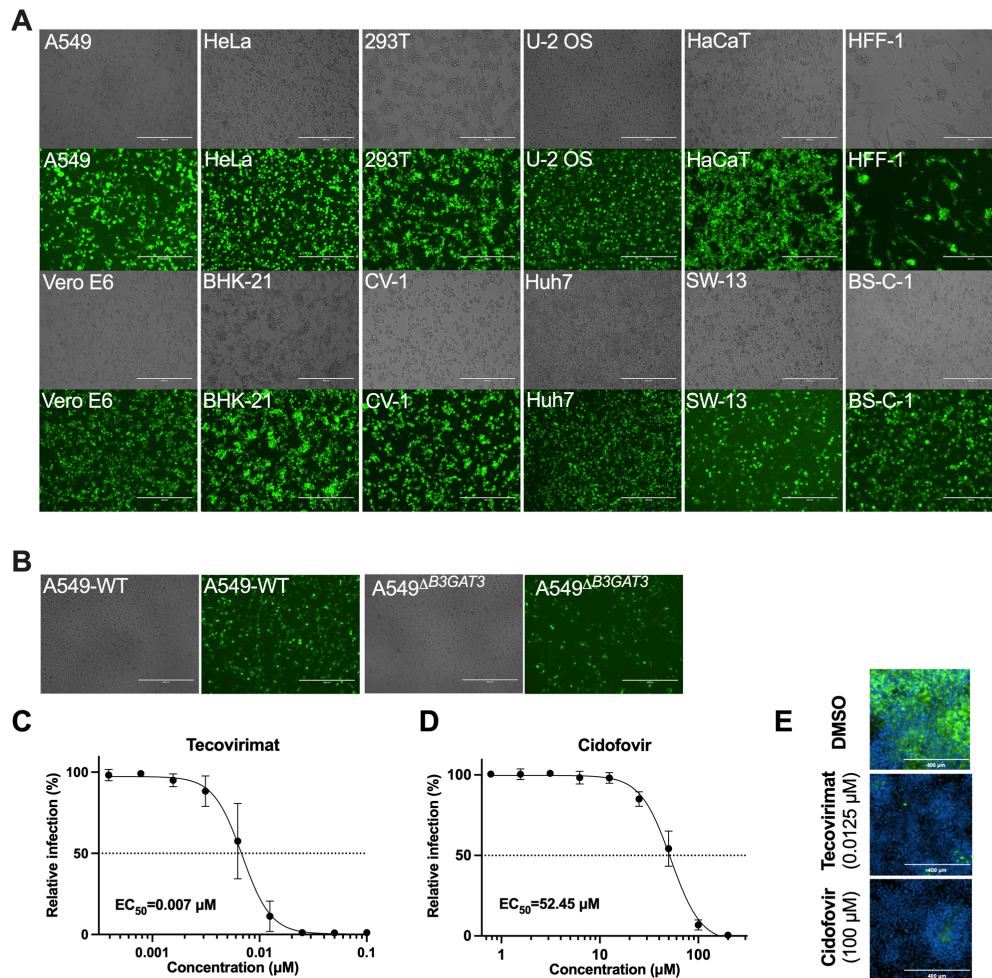
E. Read depth of P5 rdMPXV^{Δ96} aligned to rdMPXV^{Δ96} reference sequences.

F. Analysis of sequencing reads from P5 of rdMPXV^{Δ96} mapping to virus or host genome.

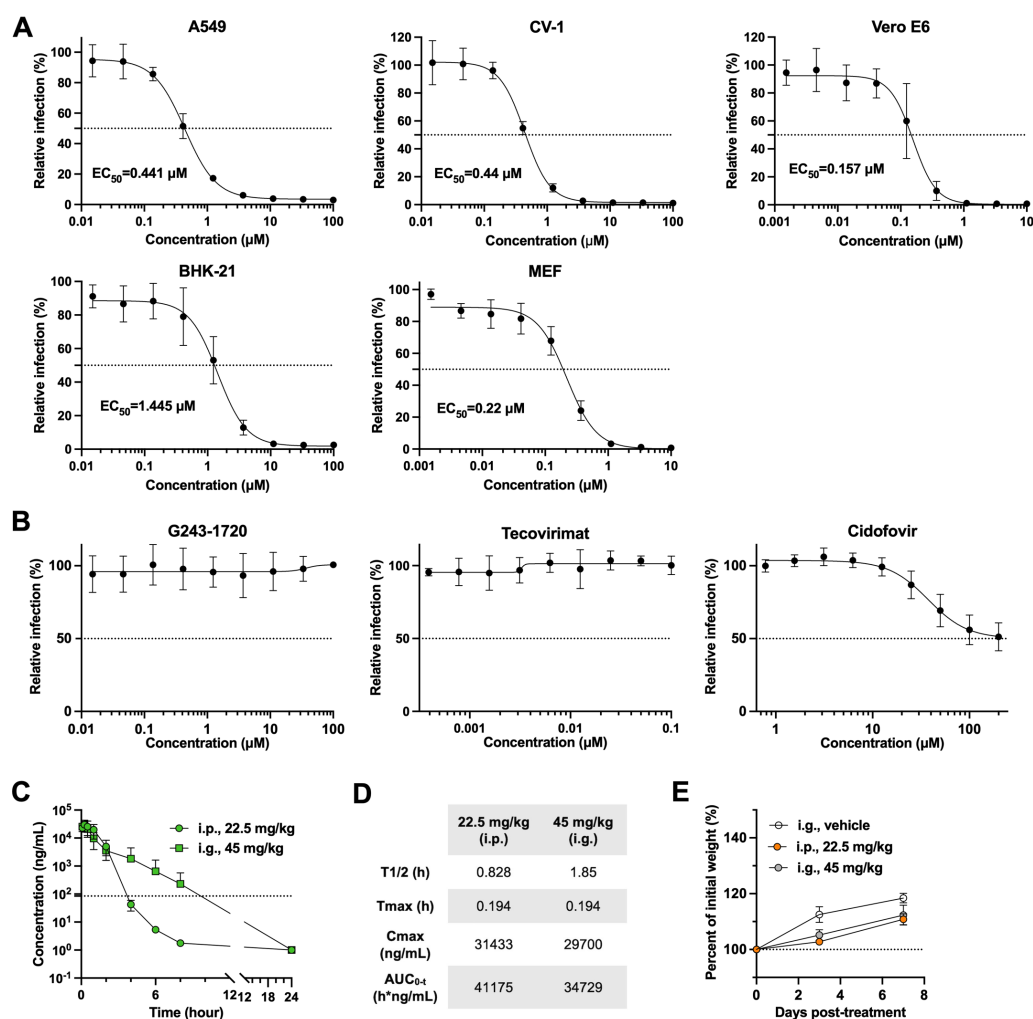


Supplementary Figure 3. Sequence verification of pBAC-I $\Delta_{96,158}$ plasmid and stability analysis of rdMPXV $\Delta_{96,158}$ upon serial passaging. **A.** Read depth of *E. coli*-derived pBAC-I $\Delta_{96,158}$ aligned to pBAC-I $\Delta_{96,158}$ reference sequences. pBAC-I $\Delta_{96,158}$ plasmid was constructed by CRISPR-based editing in combination with Lambda Red recombination. **B-C.** Read depth of *E. coli*-derived pBAC-I $\Delta_{96,158}$ aligned to the MPXV reference genome, focusing on OPG96 (B) and OPG158 (gene A32.5L) (C) and their flanking regions. **D.** Stability analysis of serially passaged rdMPXV $\Delta_{96,158}$ in CV-1-WT

and CV-1-96 cells. rdMPXV^{Δ96,158} passaged 10 times (P10) in CV-1-96,158 cells, was used to passage another three rounds in CV-1-WT and CV-1-96 cells. Brightfield and fluorescent images were captured at 96 h post-infection. Scale bar, 400 μm. **E.** PCR verification of *OPG96* and *OPG158* deletions and the mGreenLantern-P2A-Gaussia luciferase reporter cassette in P10 rdMPXV^{Δ96,158}. Viral DNA from P10 was amplified by PCR, with pBAC-I^{Δ96,158} as a positive control. **F.** Read depth of P5 (red) and P10 (green) rdMPXV^{Δ96,158} aligned to the rdMPXV^{Δ96,158} reference genome. **G-H.** Read depth of P5 (red) and P10 (green) rdMPXV^{Δ96,158} aligned to MPXV reference genome, focusing on *OPG96* (G) and *OPG158* (H) and flanking regions.

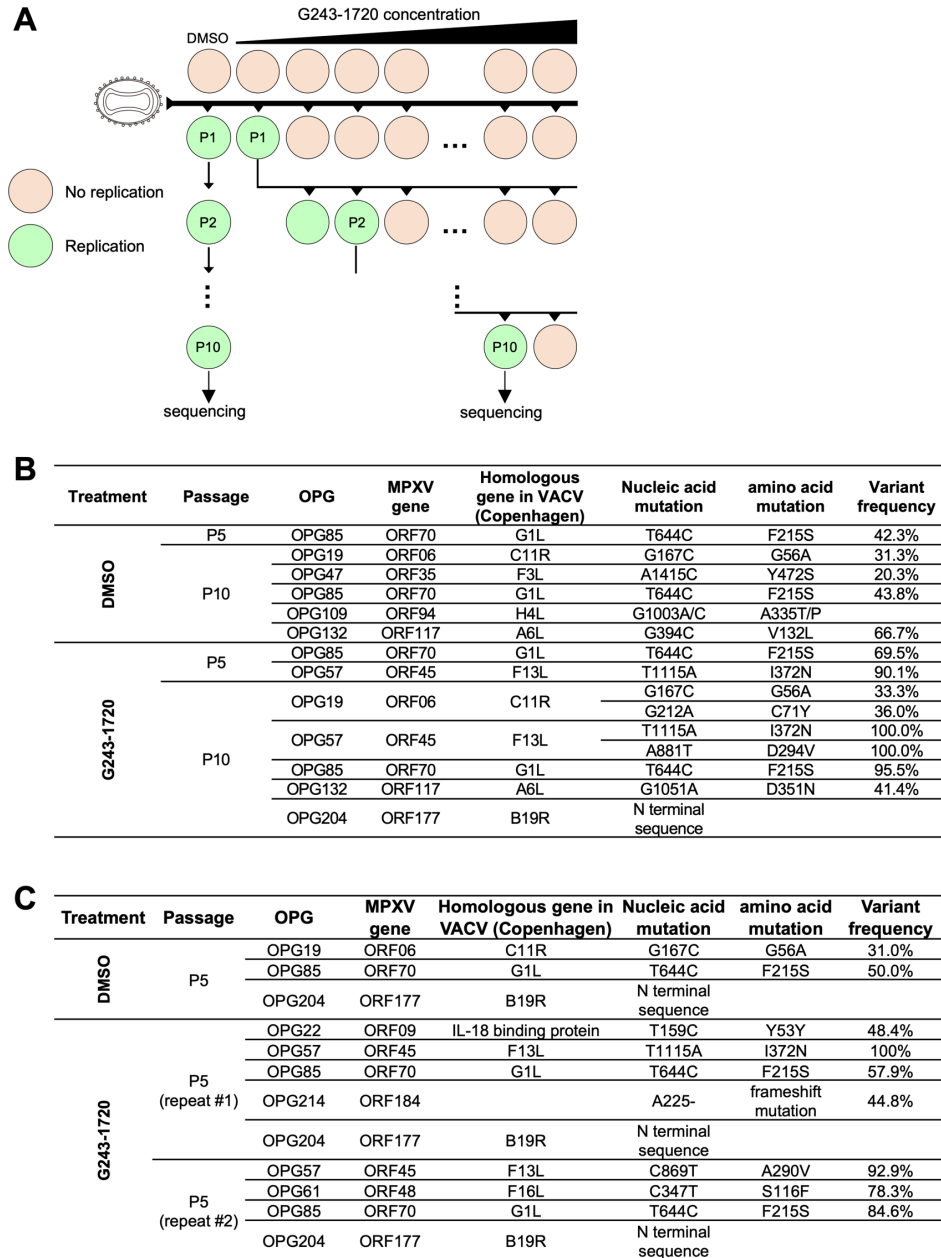


Supplementary Figure 4. Cell susceptibility and antiviral compound assessment of replication-defective $\text{rdMPXV}^{\Delta 96,158}$ particles. A. Representative images of $\text{rdMPXV}^{\Delta 96,158}$ infection in various cell lines (MOI 0.5, 48 h), as described in Figure 2H). B. Representative images of $\text{rdMPXV}^{\Delta 96,158}$ infection in WT and $\Delta B3GAT3$ A549 cells (MOI 0.5, 48 h), as described in Figure 2I. C-D. EC_{50} of tecovirimat (C) and cidofovir (D) in HaCat-96,158 cells infected with $\text{rdMPXV}^{\Delta 96,158}$ (MOI 0.1, 30 h). E. Representative fluorescence images of HaCat-96,158 cells pre-treated with tecovirimat (0.125 μM) or cidofovir (100 μM) for 1 h, followed by $\text{rdMPXV}^{\Delta 96,158}$ infection (MOI 0.1, 30 h). Cells were fixed, stained with DAPI, and imaged under a fluorescence microscope. Scale bar, 400 μm . Error bars represent standard deviations from three biological replicates ($n=3$; C and D; mean \pm s.d.).



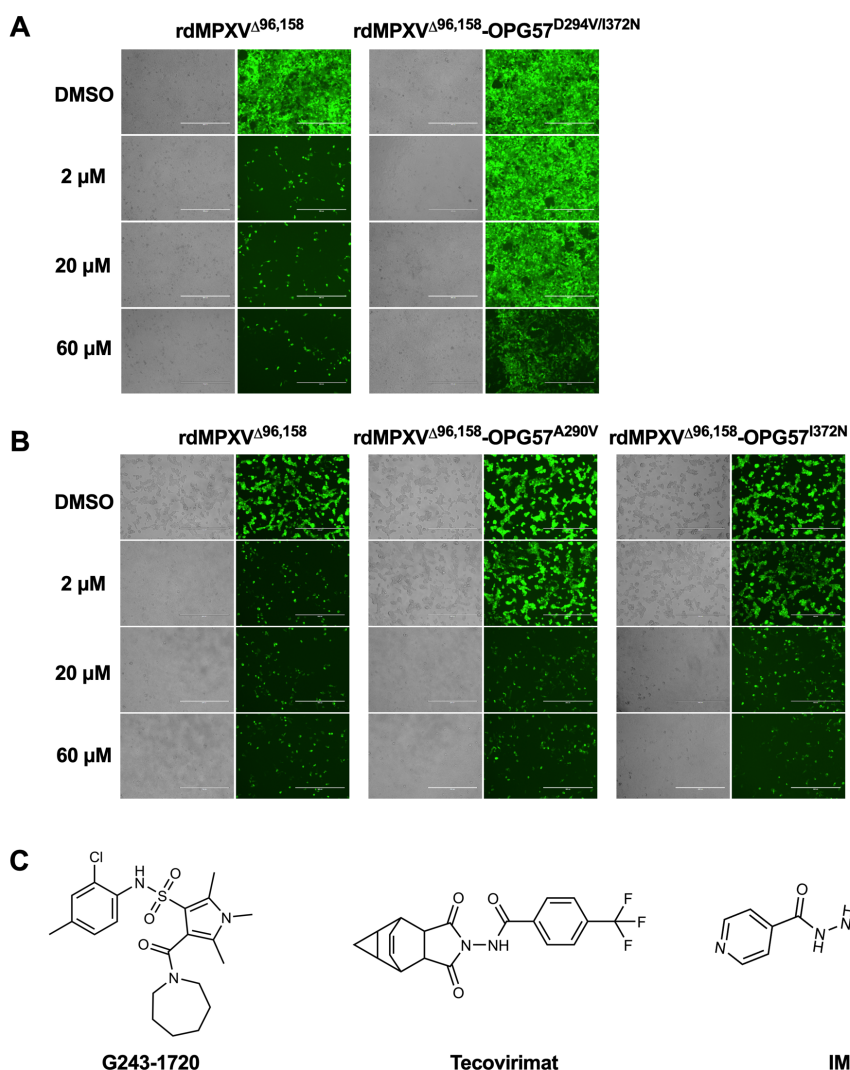
Supplementary Figure 5. Antiviral activity, pharmacokinetics, and toxicity of G243-1720. **A.** EC₅₀ of G243-1720 in VACV-infected A549, CV-1, Vero E6, BHK-21, and MEF cells (n=3). Cells were pre-treated with G243-1720 (serial dilutions starting at 100 μM) for 1 h, then infected with VACV at specified MOIs (A549 (MOI 0.0004), CV-1 (MOI 0.0004), Vero E6 (MOI 0.0005), BHK-21 (MOI 0.005), MEF (MOI 0.001)) for 36 h. **B.** Inhibition of G243-1720 in FPV-infected primary chick embryo fibroblasts (n=3). Cells were pre-treated with serially diluted G243-1720 for 1 h, then infected with FPV (MOI 0.05) for 48 h. Tecovirimat and cidofovir were used as control. **C-D.** Pharmacokinetic profile of G243-1720. Plasma concentration-time curves (B) and pharmacokinetic parameters (C) following intraperitoneal (22.5 mg/kg) or intragastric (45 mg/kg) administration to male ICR mice (n=3 per group, 4-6 weeks old). Blood samples were collected at 0.0833, 0.25, 0.5, 1, 2, 4, 6, 8, 12, and 24 h. The concentrations of G243-1720 were analyzed by LC-MS/MS (SCIEX Triple Quad 5500+

System). **E.** Toxicity assessment in uninfected severe combined immunodeficiency (SCID) mice (n=5- 6 per group, 4-5 weeks old). Mice were administered vehicle control via intragastric route twice daily, or G243-1720 via intragastric (45 mg/kg) or intraperitoneal (22.5 mg/kg) route twice daily. The body weight was recorded on day 0, 3, and 7. Error bars represent standard deviations from one (n=3 mice for C; n=5-6 mice for E; mean \pm s.d.) or three (n=3; A and B; mean \pm s.d.) independent experiments.

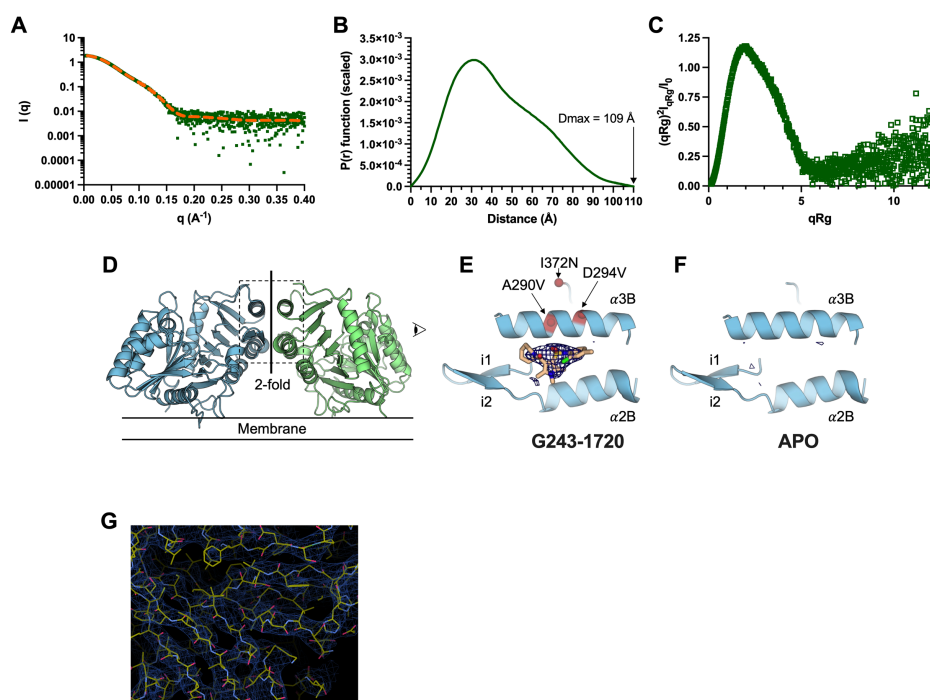


Supplementary Figure 6. Identification of G243-1720-resistant mutations in MPXV. **A.** Schematic of selecting G243-1720-resistant MPXV mutations through serial passaging in HaCat-96,158 and CV-1-96,158 cells. Cells were pre-treated with increasing concentrations of G243-1720, infected with rdMPXV^{Δ96,158}, and passaged 10 times. Viruses that are able to replicate at the highest compound concentration were selected and passaged onto new cells treated with higher concentrations of the compound. Control viruses were passaged in parallel in DMSO-treated cells. **B.** Mutations in control vs. G243-1720-resistant viruses (P5 and P10 of rdMPXV^{Δ96,158}) in HaCat-96,158 cells. **C.** Mutations in control vs. G243-1720-resistant viruses (P5 of

rdMPXV^{Δ96,158}) in CV-1-96,158 cells.



Supplementary Figure 7. Resistance of rdMPXV^{Δ96,158} mutants to G243-1720 compound. A. Resistance of rdMPXV^{Δ96,158} carrying the OPG57^{D294V/I372N} to G243-1720. HaCat-96,158 cells pre-treated with G243-1720 at varying concentrations were infected with P10 of rdMPXV^{Δ96,158} or rdMPXV^{Δ96,158}-OPG57^{D294V/I372N} at an MOI 0.05 for 48 h. Cells were fixed and imaged. B. Resistance of rdMPXV^{Δ96,158} carrying the OPG57^{A290V} or OPG57^{I372N} to G243-1720. CV-1-96,158 cells pre-treated with G243-1720 were infected with P5 of rdMPXV^{Δ96,158}, rdMPXV^{Δ96,158}-OPG57^{A294V}, or rdMPXV^{Δ96,158}-OPG57^{I372N} at an MOI 0.05 for 48 h. Cells were fixed and imaged. Scale bar, 400 μm. C. Chemical structures of G243-1720, tecovirimat, and IMCBH.



Supplementary Figure 8. SAXS analysis of sOPG057/G243-1720 and crystal structure of sOPG057/G243-1720. **A.** Guinier plot showing the experimental scattering curve of the sOPG057/G243-1720 complex in green, and the fitted curve used to generate the pair distance distribution in orange. **B.** Pair distance distribution function used to obtain Dmax and Rg values. **C.** Dimensionless (normalized) Kratky plot showing the characteristic shape of a well-folded protein. **D.** Crystal structure of the sOPG057 homodimer represented in cartoon with one protomer colored in blue and the other in green. The 2-fold axis is indicated by a black line. The dimer interface is boxed by a dashed black line. The side eye icon indicates the orientation of the close-up view used in panel B and C. **E-F.** Close-up views of the dimer interface of the crystal structure of the sOPG057 soaked with G243-1720 (E) and not soaked (F). The 2Fo-Fc map contoured at 1σ shows a clear density at the dimer interface in the soaked crystal, which is compatible with G243-1720. There is no electron density at the dimer interface in the non-soaked crystal. The three G243-1720 escape mutants (A290V, D294V and I372N) are indicated as red spheres and labelled. **G.** An image of a portion of the electron density map (contour level = 2.0, type of map = 2Fo-Fc).

Supplementary Table 1. Summary of EC50 values of antivirals and antibodies (7D11) from known studies for MPXV

Compounds	Strains	EC ₅₀ values (µM)	Cell lines	Reference
Tecovirimat	Zaire	0.01	Vero	1
	Zaire	0.008±0.0014	Vero E6	2
	MPXV-V78-I-3945	0.023±0.0026	BSC-40	3
	MPXV-V81-I-179	0.032±0.0061	BSC-40	3
	MPXV-2003-USA-039	0.036±0.0045	BSC-40	3
	MPXV-V77-I-823	0.030±0.0114	BSC-40	3
	MPXV-V1979-I-005	0.039±0.0016	BSC-40	3
	12 MPXV isolates from the outbreak in 2022	0.004-0.02	HFF and HFK	4
	SP2833	0.006±0.0002	Vero E6	2
	rdMPXV ^{Δ96,158}	0.003	CV-1-96,158	this study
Cidofovir	rdMPXV ^{Δ96,158}	0.007	HaCat-96,158	this study
	Zaire	27±11	Vero 76	5
	Zaire	5.722±0.2059	Vero E6	2
	12 MPXV isolates from the outbreak in 2022	5-32	HFF and HFK	4
	SP2833	1.980±0.0579	Vero E6	2
	rdMPXV ^{Δ96,158}	10.45	CV-1-96,158	this study
Antibody	rdMPXV ^{Δ96,158}	52.45	HaCat-96,158	this study
	Strain	EC ₅₀ value (µg/mL)	Cell line	Reference
	7D11	11b.c.1	Vero-E6	6
7D11	rdMPXV ^{Δ96,158}	0.83	CV-1-96,158	this study

Reference

1. Yang G, et al. An orally bioavailable antipoxvirus compound (ST-246) inhibits extracellular virus formation and protects mice from lethal orthopoxvirus Challenge. J Virol 79, 13139-13149 (2005).

2. Warner BM, et al. In vitro and in vivo efficacy of tecovirimat against a recently emerged 2022 monkeypox virus isolate. Sci Transl Med 14, eade7646 (2022).

3. Smith SK, Olson VA, Karem KL, Jordan R, Hruby DE, Damon IK. In vitro efficacy of ST246 against smallpox and monkeypox. Antimicrob Agents Chemother 53, 1007-1012 (2009).

4. Bojkova D, et al. Drug Sensitivity of Currently Circulating Mpox Viruses. N Engl J Med 388, 279-281 (2023).

5. Smee DF, Sidwell RW, Kefauver D, Bray M, Huggins JW. Characterization of wild-type and cidofovir-resistant strains of camelpox, cowpox, monkeypox, and vaccinia viruses. Antimicrob Agents Chemother 46, 1329-1335 (2002).

6. Yang X, et al. Identification of neutralizing nanobodies protecting against poxvirus infection. Cell Discov 11, 31 (2025).

Supplementary Table 2. Crystallographic statistics	
	F13 WT/G243-1720
PDB code:	9QQV
Data collection:	
Beamline	PROXIMA 1
Space group	F 4 3 2
Unit cell parameters:	
a,b,c (Å)	281.49
Resolution (Å)	39.42 – 3.40
Last resolution bin (Å)	3.67 – 3.40
Total observations	1077641 (222213)
Unique reflections	13691 (2755)
Completeness (%)	99.9 (100.0)
Redundancy	78.7 (80.7)
$\langle I/s \rangle$	17.7 (1.1)
R _{sym} (%)	22.3 (644.1)
CC _{1/2}	100 (76.3)
B Wilson (Å ²)	166.12
Resolution with $\langle I/s \rangle = 2$ (Å)	3.62
Refinement:	
Resolution (Å)	39.42 – 3.40
Last resolution bin (Å)	3.66 – 3.40
Number of reflections	13559 (2408)
Nb of reflections used to calculate Rfree	650 (128)
B refinement	ISOTROPIC-TLS
Rfactor (%)	21.36 (46.14)
Rfree (%)	26.54 (53.44)
Number of atoms (Mean B value in Å²):	
F13	2826 (155.33)
G243-1720	29 (181.97)
Ligands	31 (185.18)
Waters	15 (129.74)
Root mean square deviations:	
Bond lengths (Å)	0.002
Bond angles (°)	0.430
Ramachandran favored/outliers (%)	94.62/0.00

Supplementary Table 3. SAXS data collection and scattering derived parameters

Data collection parameters	
Instrument	Beamline SWING (SOLEIL)
Detector	CCD-based AVIEX
Beam geometry	0.8 mm x 0.15 mm
Wavelength (Å)	1.0
q-range (Å ⁻¹)	0.0064 < q < 0.40
Exposure time (s)	0.99
Temperature (K)	288
Structural parameters	
I(0) Guinier	1.88
R _g Guinier (Å) ^a	33.0
I(0) P(r)	1.88
R _g P(r) (Å)	33.4
D _{max} (Å)	109
Molecular mass determination	
MM _{sequence} ^b	88.6
MM _{SAXS QR} ^c	81.1
MM _{SAXS QR} ^d	78.5
^a R _g obtained with the Guinier approximation in the range qR _g < 1.3; ^b The calculated masses were derived from the sequence; ^c Molecular mass obtained from the I(q) curve (q _{max} = 0.410 Å ⁻¹) using the MoW3 program, available at http://saxs.ifsc.usp.br ; ^d Molecular mass obtained from bayesian interference analysis	

Supplementary Table 4. SAXS data					
	R_g [Å]	D_{max} [Å]	Chi ²	S [S]	f/f ₀
Experimental value					
sF13 dimer	33.0	109	ND	4.6±0.2	1.45
Models used for crysol fitting – Calculated values					
sF13 monomer	21.0	73	169	3.6	ND
sF13 dimer	32.6	118	2.34	5.2	ND